



Evolution of mining-induced water inrush disaster from a hidden fault in coal seam floor based on a coupled stress–seepage–damage model

Jianli Shao · Qi Zhang · Wenquan Zhang

Received: 3 August 2023 / Accepted: 2 April 2024
© The Author(s) 2024

Abstract Water inrush originating from hidden faults in the coal seam floor is challenging to prevent due to their concealed nature. This paper develops a coupled stress–seepage–damage model for simulating rock fracture, implemented using the finite element method. The model is validated against compression–seepage tests on rock samples, capturing realistic dynamics of shear and tensile damage as well as permeability. The model is applied to the 27305 working face of a coal mine in Shandong Province, China, revealing the evolution of water inrush caused by a hidden fault. The results indicate that as the working face progresses, both the floor damage and the internal damage within the hidden fault escalate gradually. When mining reaches 80 m, the hidden fault has been activated internally, and the depth of floor damage

reaches 13 m, which still has a certain distance from the hidden fault. At 100 m, the depth of the floor damage has stabilized, while the stress concentration at the hidden fault’s tip increases, and it begins to expand if conditions for tensile damage are met. By the time mining reaches 110 m, the hidden fault has expanded 9.2 m in length and connected with the floor damage zone, forming a water inrush channel that links the aquifer to the working face, presenting a significant water inrush risk. This work provides an intuitive approach to understanding the evolution of water inrush from a hidden fault, aiding in the prevention of water inrush disasters in practical engineering applications.

Highlights

1. A coupled stress–seepage–damage model was proposed to simulate the dynamics of hidden faults during the mining process. The model has been validated with several small-scale laboratory compression–seepage tests to demonstrate its capabilities.
2. By applying the proposed coupling model to a real-world coal mining operation, we demonstrate the process of hidden faults fracture propagation in the floor strata during the working face excavation, which might lead to a water inrush disaster.

J. Shao
School of Management Science and Engineering,
Shandong Technology and Business University,
Yantai 264005, China

J. Shao · W. Zhang
State Key Laboratory of Strata Intelligent Control
and Green Mining Co-founded By Shandong Province
and the Ministry of Science and Technology, Shandong
University of Science and Technology, Qingdao 266590,
China

Qi. Zhang (✉)
Department of Civil and Environmental Engineering, The
Hong Kong Polytechnic University, Hung Hom, Kowloon,
Hong Kong, China
e-mail: q7zhang@polyu.edu.hk

3. The most critical scenario occurs when concealed faults are positioned beneath the working face, resulting in a significant increase in the compressive stress borne by these hidden faults. This increase continues until a damaged state is reached, thereby triggering the propagation of fractures.
4. Microseismic monitoring technology proves to be an effective measure to prevent water inrush caused by hidden faults, and in our application, microseismic event distributions near the working face are consistent with our numerical analysis results.

Keywords Water inrush disasters · Stress–seepage–damage coupling model · Hidden faults · Rock failure · Underground mining

1 Introduction

In recent years, the majority of the coal mines in North China have steadily transitioned to deep mining (Lu and Wang 2015). The distance between the major coal seam and the lower Ordovician limestone aquifer is gradually shrinking, making the threat of water inrush from the bottom more and more serious (Wu et al. 2017; Li et al. 2020; Zuo et al. 2022). Although there has been an increase in awareness and focus on mine water inrush prevention recently, water inrush from the coal seam bottom still happens occasionally as a result of water inrush channels created by fault tectonic activity, causing in casualties and huge economic losses (Wang et al. 2018; Hu et al. 2019; Liang and Song 2021). Therefore, it has become crucial to figure out how to properly avoid and prevent water inrush from the floor caused by faults.

Many scholars have studied the mechanism of water inrush from faults extensively in previous decades. Cheng et al. (2013) systematically analyzed the regularity of plastic failure of rock mass caused by fault inclination, the width of the fault fractured zone, and aquifer pressure. The water inrush channel, however, is created by the propagation of mining fissures rather than the rock mass entering the plastic deformation stage (Zhang et al. 2019). Zhao et al. (2020a) observed the dynamic response process of the fault structure under mining conditions, including

slip velocity, slip distance, and friction force, and then analyzed the turning and failure process of the fault structure. Qian et al. (2018) investigated the evolution of fault water inrush accident in the Tianzhuang Coal Mine of Shandong Province and finally found that groundwater in the Ordovician limestone aquifer below the floor of 28.5 m flows into the roadway through the fault. Fault activation during mining is believed to be the key to the occurrence of water inrush disasters (Zhang et al. 2014; Hu et al. 2019). It has also been shown that changes in the pore structure of the rock mass inside the fault occur under engineering disturbance, resulting in enhanced seepage, which is one of the reasons for the occurrence of water inrush disasters (Liu et al. 2019; Kong and Wang 2020; Ma et al. 2022). Zhao et al. (2020b) constructed a numerical model of Darcy–Forchheimer flow in the aquifers, fault zones, and fracture zones to analyze the non-Darcy flow characteristics after fault water inrush. These works have consistently enhanced and expanded the understanding of water inrush mechanisms. However, the understanding of water inrush from hidden faults with shallow growth horizons in the floor, which are challenging to detect, remains inadequate.

The key to water inrush from hidden faults, in contrast to the usual mechanism of water inrush from faults, lies in the water inrush channel formed by the fracture propagation of hidden faults breaking through the water barrier under mining effect (Sun et al. 2019). Using the extended finite element method and fracture mechanics, Zhou et al. (2018) performed numerical simulations to quantitatively investigate the stress field at the fault tip and then evaluated the possibility of water inrush due to fault activation. Du et al. (2021) employed the finite difference method to simulate the seepage process of a hidden fault under the combined action of high-ground stress and confined water. Since the formation of water inrush channel cannot be intuitively understood, these studies have not yet fully recognized the water inrush catastrophe process of hidden faults in coal seam floor. As a result, there are still significant challenges in the prevention of water inrush from hidden faults.

For the process of water inrush from a hidden fault, the actual evolution is the initiation and propagation of the hidden fault under the coupled effect of mining stress and confined water, which involves the multi-field coupling phenomenon of rock stress,

seepage, and damage (Li et al. 2021; Zhao et al. 2022; Liu et al. 2022). Based on the traditional elastoplasticity theory and numerical methods for continua without discontinuity, it is difficult to visually observe the process of the hidden fault extension, much less to thoroughly study the water inrush mechanism (Li et al. 2011; Lu and Wang 2015; Shao et al. 2022). Therefore, it is essential to establish a numerical model applicable to fracture propagation under the stress–seepage coupling effect and accurately reflect the water inrush channel development of hidden faults under hydraulic-mechanical interaction.

This paper presents a fully coupled stress–seepage–damage numerical model for brittle rock materials at first. Secondly, two compression-seepage cases for rock samples are used to validate the process of crack propagation and seepage. Finally, the simulation of the evolution process of water inrush disaster caused by a hidden fault during coal mining is conducted based on the site conditions. The analysis examines the stress distribution in the floor, the activity of the hidden fault, and the development of the water inrush channel. The findings can serve as a reference for preventing water inrush from the floor caused by hidden faults.

2 A coupled stress–seepage–damage model for brittle rock materials

2.1 Heterogeneity hypothesis for rock materials

Rock materials are composed of mineral crystal particles, micro defects, and cementing materials in different arrangements, which results in the non-uniform distribution of mechanical properties of rock elements over the material space, and this non-homogeneity is of great importance for their localized rupture phenomena (Chen et al. 2004; Yang et al. 2004). In this paper, a statistical-mathematical approach is used to assign physical–mechanical parameters to rock materials and to translate the non-homogeneous constitutive characteristics of rock materials into macroscopic material properties.

Among the many probability distribution functions on the heterogeneity of rock materials, the Weibull distribution (Weibull 1951), which is now widely recognized, plays an important role in the study of the deformation of rock materials. In this paper, it is

assumed that the physical–mechanical properties of fine elements in material space fit the Weibull distribution, and the probability density of the distribution is:

$$F(u) = \frac{m}{u_0} \left(\frac{u}{u_0} \right)^{m-1} \exp \left[- \left(\frac{u}{u_0} \right)^m \right] \quad (1)$$

where u is a certain property, which is Young's modulus in this paper; u_0 is a scale parameter, which is related to the mean value of the property; and m is a shape parameter, which is positively related to the homogeneity of rock materials. Figure 1 shows the probability density with different shape parameters m .

2.2 Statistical damage constitutive model

The element damage is assumed to conform to the one-dimensional linear elasticity law (Lemaitre 1985; Jirásek and Bauer 2012), which can be described as follows:

$$\sigma = E\varepsilon = E_0(1 - D)\varepsilon \quad (2)$$

where σ is stress, E and E_0 are Young's moduli for damaged and undamaged materials, respectively, ε is the elastic strain, and D is the damage variable. To avoid the problem caused by the zero Young's modulus, when $D=1.0$, the Young's modulus of the damage element is designated as a very small value, such as 1.0×10^{-5} MPa (Xu et al. 2017).

The damage constitutive relation of an element under uniaxial compressive and tensile stress is illustrated in Fig. 2. Initially, the element is

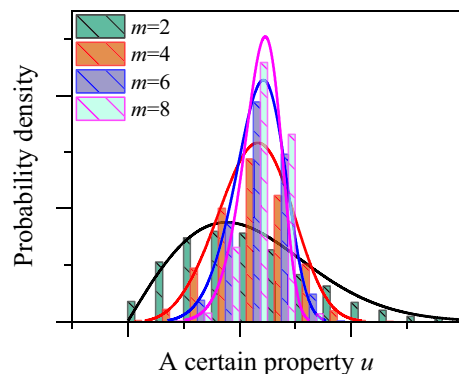


Fig. 1 Probability density for a certain property with different shape parameters

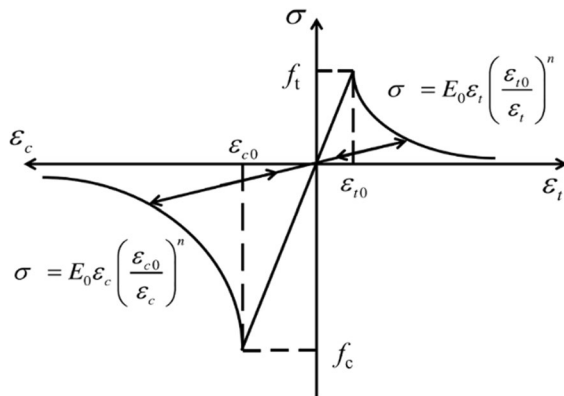


Fig. 2 Typical stress–strain relationship of rock

considered elastic with the given properties defined by Young’s modulus and Poisson’s ratio. The stress is proportional to the axial strain before the damage. Once the given damage threshold is attained, the stress–strain relation of the element is modified by softening.

The tensile failure criterion is determined by the maximum tensile-stress criterion, while the shear failure criterion is determined by the Mohr–Coulomb criterion, as follows (Chen et al. 2018):

$$\begin{cases} F_1 = \sigma_1 - f_t \\ F_2 = -\sigma_3 + \sigma_1 \left(\frac{1 + \sin \varphi}{1 - \sin \varphi} \right) - f_c \end{cases} \quad (3)$$

where σ_1 is the maximum principal stress, σ_3 is the minimum principal stress, f_t is the tensile strength, f_c is the compressive strength that depends on the material’s cohesion magnitude, and φ is the internal friction angle. Under the compressive or tensile yield condition, the damage variable of the element is expressed as (Tang et al. 2008):

$$D = \begin{cases} 0, & 0 \leq \varepsilon_t < \varepsilon_{t0} \\ 1 - (\varepsilon_{t0}/\varepsilon_t)^2, & \varepsilon_t \geq \varepsilon_{t0} \\ 0, & \varepsilon_{c0} < \varepsilon_c < 0 \\ 1 - (\varepsilon_{c0}/\varepsilon_c)^2, & \varepsilon_c \leq \varepsilon_{c0} \end{cases} \quad (4)$$

where ε_{t0} is the elastic limit tensile strain, ε_{c0} is the elastic limit compressive strain, ε_c is the minimum principal strain, and ε_t is the maximum principal strain. For the case of multi-axial stress, ε_t is equal

to the equivalent principal strain in the tensile state, which can be expressed as follows:

$$\varepsilon_t = \sqrt{\langle \varepsilon_1 \rangle^2 + \langle \varepsilon_2 \rangle^2 + \langle \varepsilon_3 \rangle^2} \quad (5)$$

where

$$\langle x \rangle = \begin{cases} x, & x \geq 0 \\ 0, & x < 0 \end{cases} \quad (6)$$

is the so-called Macaulay bracket.

2.3 The coupled stress–seepage–damage relation

The mechanical equilibrium of a porous rock is governed by the following equation assuming a quasi-static condition:

$$\sigma_{ij,i} + F_j = 0 \quad (7)$$

where σ_{ij} denotes the total Cauchy stress tensor and F_j denotes the body force vector. We also have the geometrical compatibility relation that determine the strain field from the displacement field assuming small deformation, as shown below:

$$\varepsilon_{ij} = \frac{1}{2} (u_{i,j} + u_{j,i}) \quad (8)$$

where ε_{ij} denotes the infinitesimal strain tensor and u_i is the displacement vector. As the constitutive model predicts the effective stress tensor from a given strain tensor, we need another equation to relate the effective stress tensor with the total stress tensor, a fundamental result of poroelasticity theory and mixture theory, which is given as (Lei et al. 2021):

$$\sigma'_{ij} = \sigma_{ij} + \alpha \delta_{ij} p \quad (9)$$

where σ'_{ij} represents the effective stress tensor, p is the pore fluid pressure, δ_{ij} is the Kronecker delta, and α is the Biot’s coefficient.

Based on the mass conservation equation of the fluid flow and the Darcy’s law, the isothermal seepage equation considering the solid deformation can be derived as (Chen et al. 2017):

$$\frac{k}{\mu} \nabla^2 p = \frac{1}{S} \frac{\partial p}{\partial t} + \alpha \frac{\partial \varepsilon_v}{\partial t} \quad (10)$$

where $1/S$ is the storage coefficient (Zhang and Borja 2021), k is the permeability, and μ is the fluid

viscosity. For rock material, the porosity can be updated through the empirical equation (Rutqvist et al. 2002):

$$\phi = \phi_r + (\phi_0 - \phi_r) \exp(-\zeta \bar{\sigma}') \quad (11)$$

where ϕ_0 is the initial porosity, ϕ_r is the residual porosity, $\bar{\sigma}' = -(\sigma'_{xx} + \sigma'_{yy} + \sigma'_{zz})/3$ is the mean effective compressive stress (compression is positive), and ζ is the porosity-stress correlation coefficient.

Finally, when the damage and gradual failure of the element converges into a crack, the permeability of the crack would be at least one order of magnitude higher than the porous matrix permeability, and the change of permeability can be expressed using (Tang et al. 2002, 2008; Zhu and Wei 2011):

$$k = k_0 \left(\frac{\phi}{\phi_0} \right)^3 \exp(\alpha_k D) \quad (12)$$

where k_0 is initial permeability and α_k is the mutation coefficient of permeability.

2.4 Model implementation

The model describes the coupling relationship between mechanical deformation, seepage, and damage, and the correlation terms between the coupling of each physical field are shown in Fig. 3. The stress field governing equation includes the pore fluid pressure term, and the seepage field governing equation includes the deformation term and the effective stress term, which realizes the bi-directional coupling between the stress field and the seepage field. The damage state variables are calculated based on the effective stress and strain under stress–seepage coupling, and the permeability change and mechanical

property weakening caused by the damage effect are output to the seepage field and stress field, respectively, which realizes the full coupling relationship of each physical field.

The finite element method is used to implement the model by discretizing the problem domain into numerous cells through meshing. New failure is simulated by the damage in elements, and the damage state of the material, as well as the changes in the mechanical and permeability properties caused by the damage, are continuously updated by loading steps, based on the traditional framework of fully coupled deformation and pore pressure fields. Figure 4 illustrates a flow chart of the model. The basic procedures may be summarized as follows:

- After establishing the geometric model, parameter assignments are made and Young's modulus obeying Weibull distribution is generated.
- The task is to add solid mechanics and Darcy's law physical fields and to define statements for the calculation of damage state variables and their coupling influence relationships. Then, we set the appropriate boundary conditions and coupling interfaces. Furthermore, we set the solution step according to the loading objective and run the solution after meshing.
- After completing the first step of the solution, a damage judgment is made based solely on the stress state at that point. If the stress state does not meet the maximum tensile stress criterion or the Mohr–Coulomb yield criterion, the next load is applied directly. Conversely, if the stress state of a unit meets the damage criterion, the corresponding damage variables are calculated and material parameters such as Young's modulus and permeability are updated accordingly. After updating, the calculation is performed again under the current conditions. If new damage occurs in some elements due to changes in the material properties, the material properties are updated again. This cycle of calculations is repeated until no new damage variables are added, indicating that the damage development has stabilized under the current conditions and the current solution step is complete.
- Proceed to the subsequent loading step, and in case a novel damage variable emerges, iterate the procedure (c) until no further damage is gener-

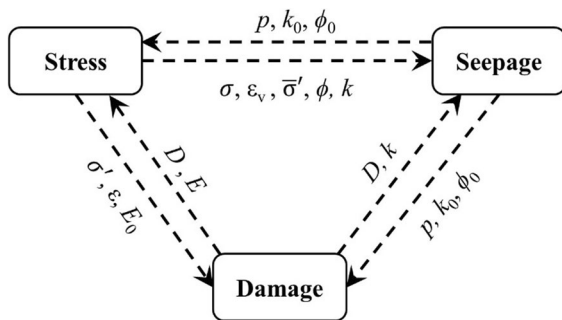
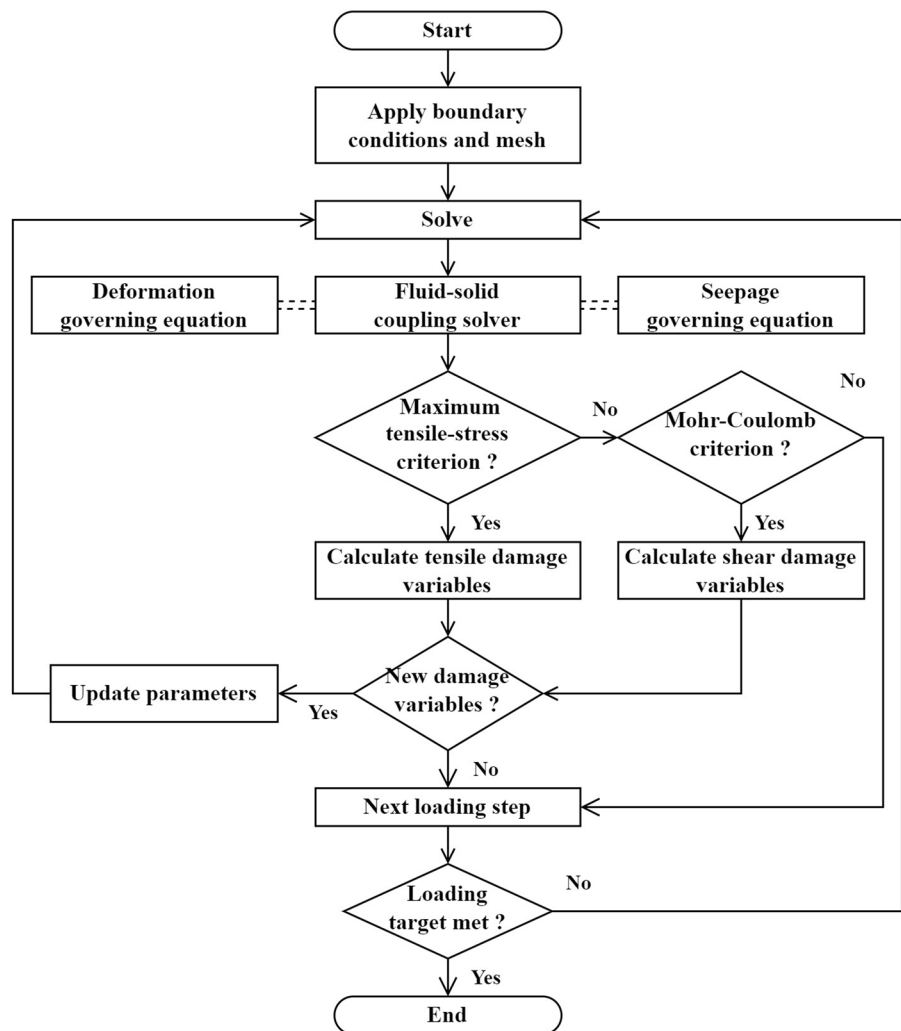


Fig. 3 Coupling relations of the model

Fig. 4 A flow chart of the model

ated. By gradually following this process until the loading target is met, the progressive rock failure under the fully coupled stress–seepage–damage condition is simulated.

2.5 Model validation

To verify the model, two cases of rock samples under compression–seepage conditions are modeled. One is an intact rock sample, and the other is a rock sample with a pre-existing fracture. By default, the saturated fluid is assumed to be water.

2.5.1 Biaxial compression tests on intact rock samples under coupled stress–seepage conditions

The two-dimensional model for a sample in the compression–seepage process is shown in Fig. 5, and the geometric size is 50 mm × 100 mm. The left and right boundaries of the model are subjected to a constant confining pressure $\sigma_3 = 5$ MPa, the bottom is restrained from vertical displacement. The top is applied with prescribed axial displacement to control the loading, and the displacement is gradually

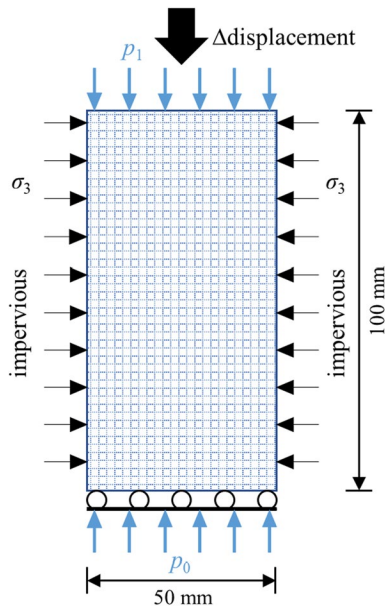


Fig. 5 Two-dimensional model for an intact rock sample

Table 1 Material properties for numerical simulation

Material properties	Value	Units
Young's modulus E (mean value)	12	GPa
Poisson's ratio ν	0.32	
Friction angle φ	30	°
Compressive strength f_c	105	MPa
Tensile strength f_t	10	MPa
Initial permeability k_0	10^{-15}	m^2
Initial porosity ϕ_0	0.01	
Mutation coefficient α_k	5	
Biot's coefficient α_B	0.2	
Shape parameter m	6	

increased by 0.001 mm per step until the sample loses its bearing capacity due to instability and failure. For steady-state seepage, the left and right boundaries of the model are impervious, the lower boundary (upstream of seepage) is subjected to constant pore fluid pressure $p_0=3$ MPa, and the upper boundary (downstream of seepage) is subjected to pore fluid pressure of 0. To characterize the heterogeneity of rock materials, the initial Young's modulus is given to fit the Weibull distribution. The calculation parameters used are shown in Table 1.

Figure 6 depicts the distribution of damage to a rock sample during axial compression, demonstrating the evolution of damage and fracture within the rock sample. Once the load reaches a certain threshold, randomly distributed damage units begin to appear within the rock sample due to its heterogeneity material properties. As displacement loading continues, the number of damaged elements gradually increases and becomes denser at a displacement of 0.864 mm, although the damage values remain small. At the displacement reached 0.944 mm, the damage value of individual elements gradually increased, and some damaged elements began to connect and merge, indicating the propagation and connection of microcracks in the rock sample. At the 1.024 mm displacement, an obviously damaged band with an oblique cut is formed, and its value reached 1.0, indicating completely broken. Based on the damage judgment, the main failure was due to shear. Finally, the rock sample loses its stability and forms a macro fracture zone, which is consistent with the failure modes observed in the studies (Lu et al. 2013; Chen et al. 2017; Li and Liu 2021), suggesting that the model used can effectively simulate the damage phenomena of rocks under compression.

Figure 7 depicts the evolution of the flow velocity during loading. Initially, the distribution of flow velocity is mainly low. Some individual elements have high flow velocity due to damage and updated permeability, but overall flow velocity remains small because there is no interconnected seepage path. At a displacement of 0.944 mm, the damaged elements gradually connect with each other. When the displacement reached 1.024 mm, the rock sample broke to form a macro seepage channel, and the flow velocity increased significantly. In the outer area, the flow is slow due to its low local permeability, but the overall flow velocity increases.

To further calibrate the simulation results, the stress–strain curves and strain–permeability curves of the numerical simulations were plotted and compared with the data of triaxial compression tests under different conditions in the previous studies, as shown in Fig. 8. It can be seen that under all these stress and pore fluid pressure coupling conditions, the trends of stress–strain curves and strain–permeability are consistent with the previous studies. Among them,

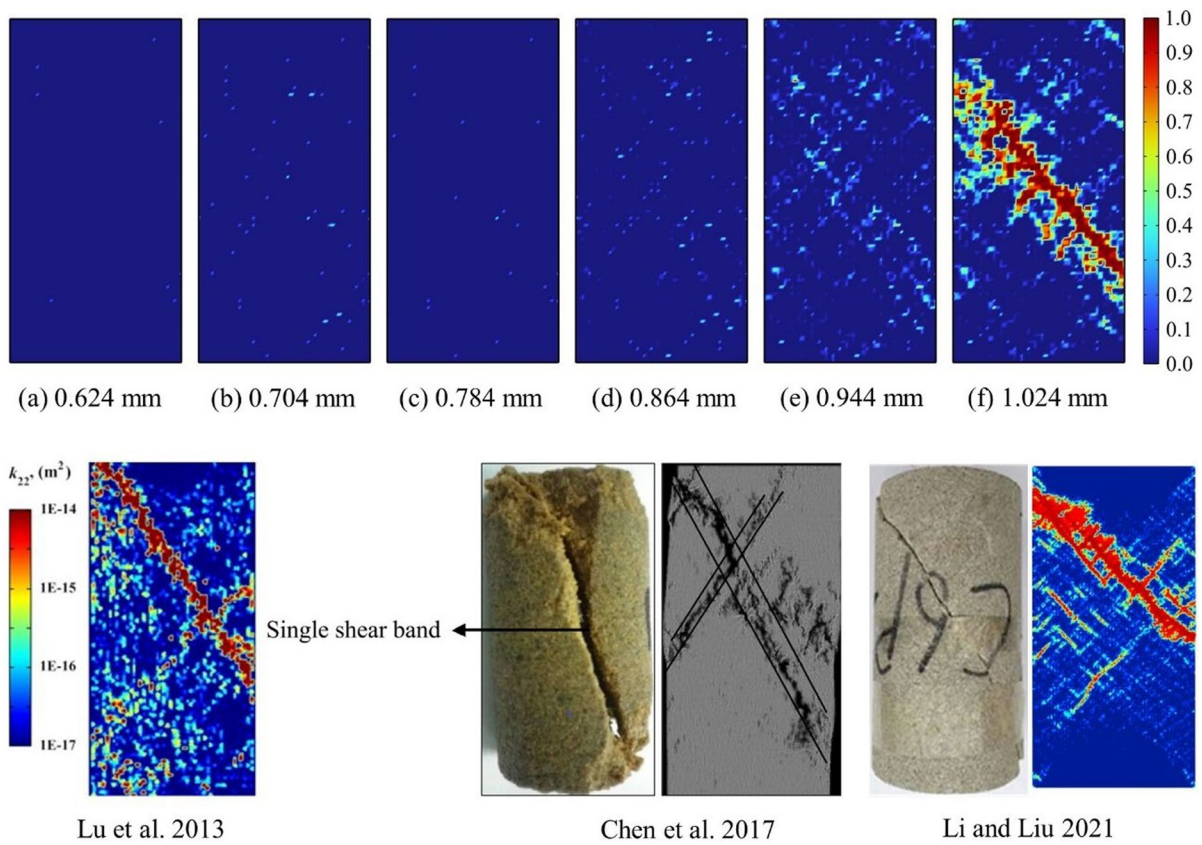


Fig. 6 Damage distribution during compression and a comparison with existing studies (Lu et al. 2013; Chen et al. 2017; Li and Liu 2021)

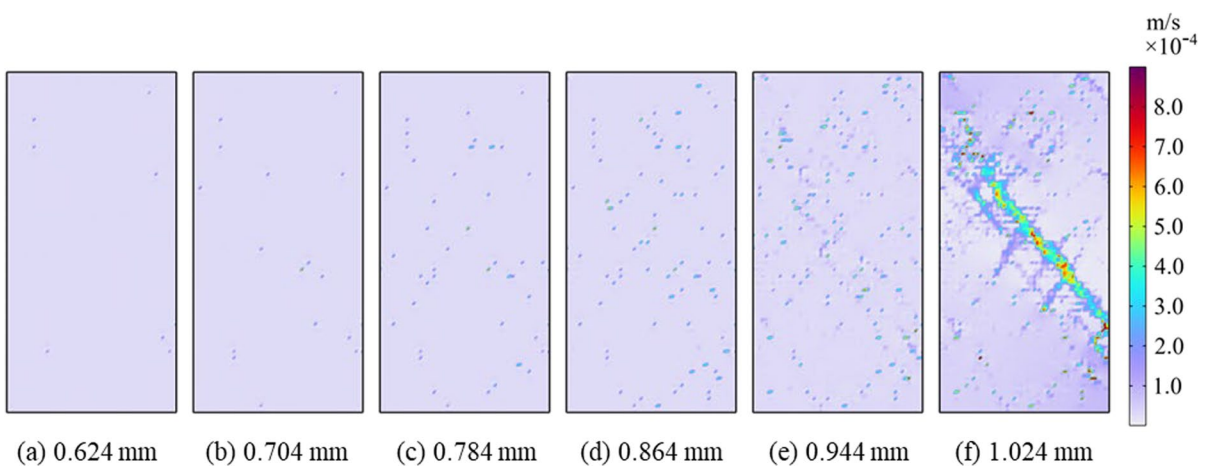


Fig. 7 Distribution of flow velocity magnitude during compression

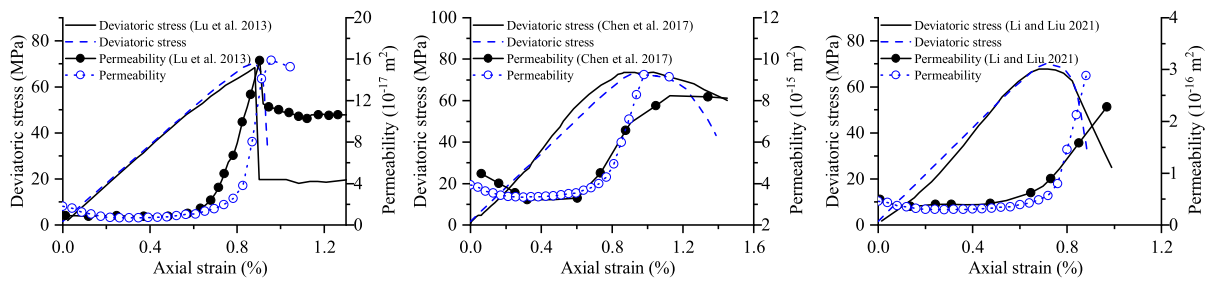


Fig. 8 Comparison of the numerical simulation results with existing studies that contain different confining pressures and pore pressure differences. The matching is achieved by fine-

tuning several material parameters such as the shape parameter and mutation coefficient

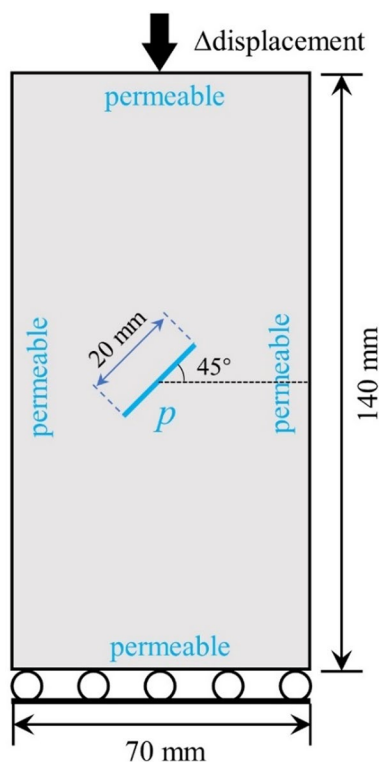


Fig. 9 Two-dimensional model for a rock sample with one pre-existing fracture

the permeability shows a slight decrease with the increase of axial strain and then a sharp increase near the peak stress. The feasibility of the coupled stress-permeability-damage model established in this paper is verified.

Table 2 Parameters used for numerical model

Parameters	Values	Units
Young's modulus E (mean value)	10.2	GPa
Poisson's ratio ν	0.14	
Density ρ	2260	kg/m ³
Internal friction angle ϕ	54	°
Compressive strength f_c	40.26	MPa
Tensile strength f_t	2.2	MPa
Permeability k	10^{-18}	m ²
Porosity ϕ	0.08	
Heterogeneity m	10	

2.5.2 Uniaxial compression tests on rock samples with pre-existing fracture under coupled stress-seepage conditions

According to the works by Wei et al. (2021), numerical simulations for uniaxial compression with different fluid pressures in a pre-existing fracture are carried out. As shown in Fig. 9, a rectangular rock-like sample with size of 70×140 mm contains a pre-existing fracture with an inclination angle of 45° and a length of 20 mm. Four water injection pressures are applied in the pre-existing fracture: 0, 0.5, 1 and 2 MPa. Displacement is applied to the top of the sample at a rate of 0.001 mm per step, and the bottom is constrained to have zero vertical displacement. Fluid pressure is applied to the pre-existing fracture boundaries. The surrounding boundaries of the sample are permeable. The average mechanical parameters of the rock-like samples used are shown in Table 2.

Fig. 10 Numerical simulation data for different fluid pressures and a comparison with experiment

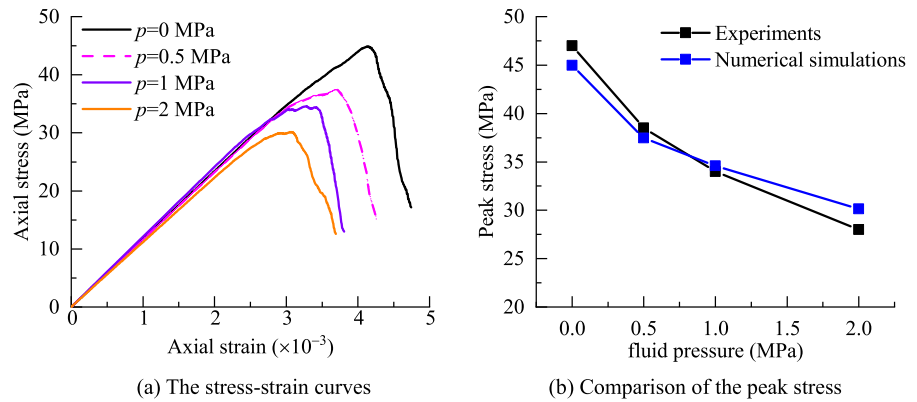
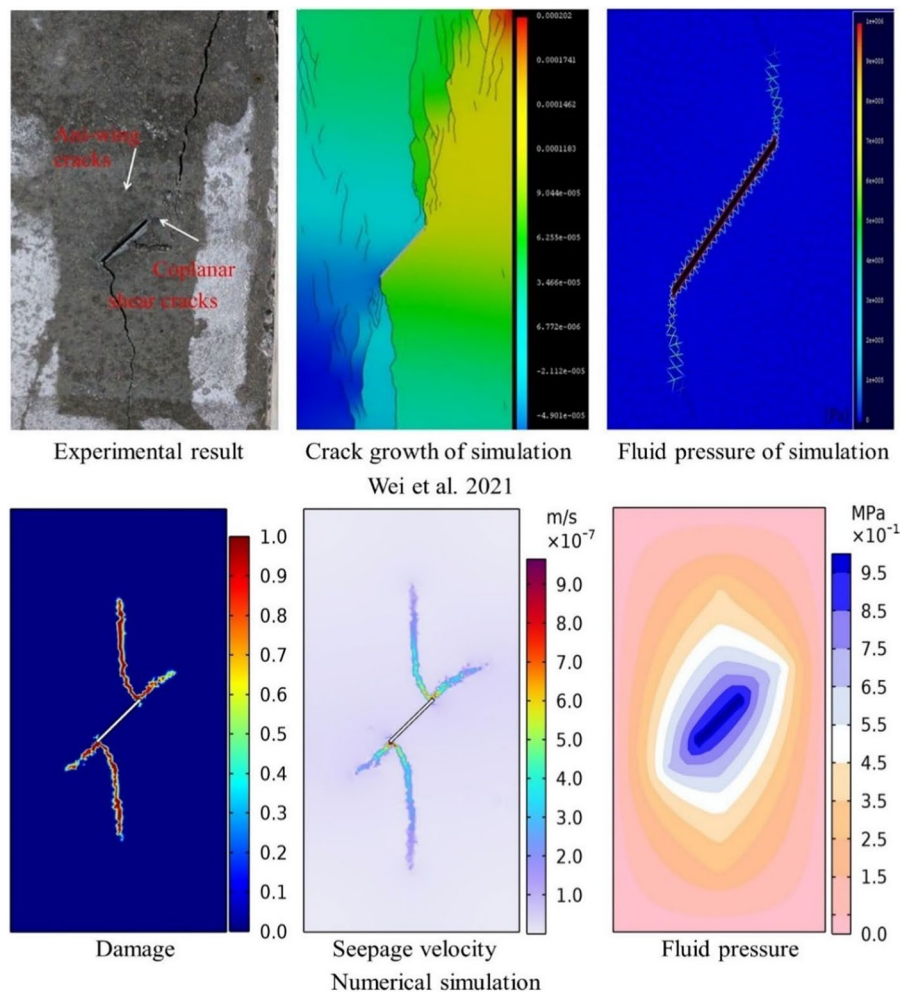


Figure 10 depicts the comparison of stress–strain curves and peak stress with different fluid pressures between experimental and numerical results. From

the stress–strain curves in Fig. 10a, the uniaxial compressive strength in numerical simulation decreases with the increase of fluid pressure, which is consistent

Fig. 11 Comparison of numerical simulation results with the existing studies (Wei et al. 2021)



with the trend observed by Wei et al. (2021). Comparing the peak strength with the experimental data, as shown in Fig. 10b, the numerical solutions are in good agreement with the experimental results, which further verifies the proposed numerical model for rock fracture propagation under hydro-mechanical interaction.

These experimental phenomena are further illustrated with the working conditions at a fluid pressure of 1 MPa, as shown in Fig. 11. It was observed that the wing cracks first propagated at the tip of the pre-existing fracture (Wang et al. 2022, 2024) and then secondary cracks were generated. As the loading progresses, the wing cracks generated at the tip of the pre-existing fracture rapidly extend to the sample surface, which eventually leads to the tensile damage of the rock sample, which is consistent with the results of this paper. Meanwhile, both can be found that the increase of fluid pressure promotes the propagation and expansion of wing cracks, which leads to the reduction of sample strength. In addition, in terms of the seepage field, the fluid passes through the cracks at a high velocity due to the significantly huge permeability of the cracks compared to the rock matrix. As a result, the fluid pressure gradually decreases from

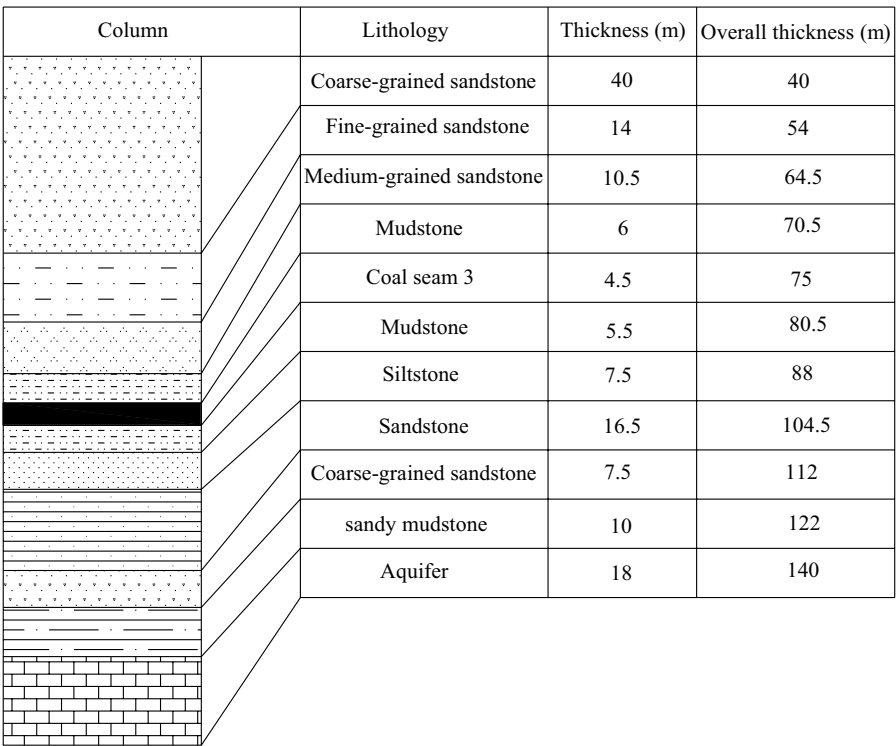
the pre-existing fracture along the generated cracks to its tip, which is also consistent with the existing study (Wei et al. 2021).

3 Modeling mining-induced water inrush from a hidden fault in coal seam floor

3.1 Engineering background

A certain mine in Jining has a design production capacity of 900,000 tons/year. The 27305 fully mechanized working face is the fourth working face in mining area 7. The ground elevation is +33.5 m ~ +34 m, the working face elevation is −1110 m to −1090 m, the designed strike length of the coal seam is 960 m, the average width is 160 m, the average thickness of the coal seam is 4.5 m, and the dip angle of the coal seam is 4°–9°. According to the exposure of the mining face, there is no obvious fold structure in the 27305 working face, but the geophysical exploration results show that there are hidden faults in the coal seam floor. When connecting with the underlying confined aquifer, it poses a certain threat to the safe mining of Coal Seam 3. The geological conditions of

Fig. 12 Geological section of working face 27305



the 27305 working face of this coal seam are shown in Fig. 12.

According to the above analysis, during the mining process of the working face, the stress distribution changes dynamically. On the one hand, the coal seam floor rock stratum produces compression-shear fracture under the advanced abutment pressure, and the shallow part of the floor unloads and expands towards the free face, resulting in tensile fracture, which continues to develop and together form the water-conducting failure zone of the floor. On the other hand, due to the synergetic effect of the gradually increasing vertical stress of the floor and confined water, the hidden fault in the floor is very easy to activate and propagate, causing longitudinal expansion. When the hidden fault extends to the floor failure zone, the dominant seepage path connecting the mining space and the Ordovician limestone aquifer is formed, thus completing the development of the water inrush channel of the hidden fault on the floor, causing water inrush disasters.

3.2 Model setup

According to the geological conditions of the study area and the actual size of the working face, a three-dimensional numerical model for mining the 27305 working face was built in the COMSOL Multiphysics software, as shown in Fig. 13. Due to the large burial depth of the working face, in order to simplify the calculation, the overlying rock strata within a certain height above the working face are used to establish

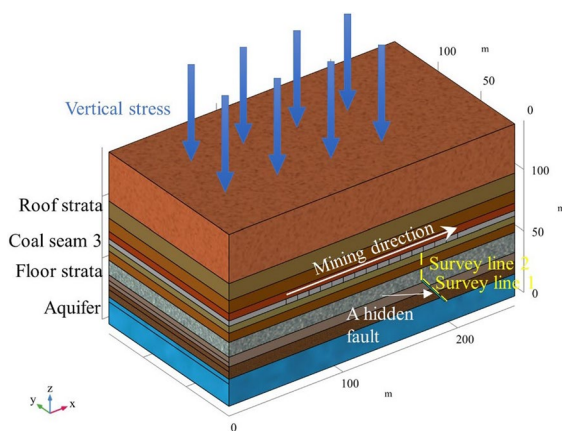


Fig. 13 The three-dimensional numerical model

a model, and the gravity of the overlying rock strata outside the height is applied to the top of the model in the form of an equivalent load. The geometric dimension of the model is 240 m×140 m×140 m, and 309,659 units are divided into grids. The coal seam is distributed nearly horizontally with a thickness of 4.5 m. There is a concealed fault in the coal seam floor, with a width of 1 m, a length of 32 m, and a dip angle of 40°. The upper end tapers off into the floor sandstone, about 22 m away from the coal seam, and the lower end is connected to the limestone aquifer.

The vertical uniform load of 15 MPa is applied to the top boundary of the model to represent the weight of the overlying rock strata, and the bottom boundary is fixed. The front, rear, left, and right boundaries of the model are supported by rollers that have zero horizontal displacement. At the same time, to simulate the stress–seepage coupling effect, the fluid pressure of the confined aquifer is set as 4 MPa, the boundary of the goaf has an atmospheric pressure, and the others are impermeable boundaries. To observe the stress changes of hidden faults in the mining process of the working face, two survey lines are set. Survey line 1 is arranged inside the fault along the direction of the hidden fault, and survey line 2 is vertically arranged to the bottom interface of the coal seam along the pinch out of the upper end of the hidden fault. The simulated total mining length is 150 m, and an iterative calculation is conducted for every 10 m mining step. According to the geological data, Table 3 lists the mechanical properties of each rock stratum used. In the model, the fluid in the seepage field is chosen to be water, with a density of 1000 kg/m³ and a viscosity of 0.001 Pa·s. The other required calculation parameters are shown in Table 4.

4 Results

4.1 Distribution of stress

The effective stress transfer interaction is adopted in the stress–seepage coupling model, and the effective stress can reflect the compression or tension state of rock mass under the influence of seepage pressure. Figure 14 shows the spatial distribution of effective stress of rock mass during coal seam mining. It can be seen from the figure that as the working face advances, due to the unloading effect, the stress

Table 3 Mechanical properties of rock strata

Strata	Young's modulus (GPa)	Poisson's ratio	Friction angle (°)	Compressive strength (MPa)	Tensile strength (MPa)	Density (kg/m ³)	Shape parameter
Roof	24	0.25	32	30	2.5	2720	6
Hidden fault	3	0.30	24	8	1	2000	3
Coal seam	10	0.28	30	20	2	1400	6
Floor	24	0.25	30	26	1.5	2650	6
Aquifer	18	0.26	32	45	3.6	2760	5

Table 4 Seepage properties of rock strata

Strata	Initial porosity	Initial permeability (m ²)	Biot's coefficient	Mutation coefficient
Roof	0.01	2.2×10^{-14}	0.3	5
Hidden fault	0.10	2.1×10^{-13}	0.5	3
Coal seam	0.01	4.1×10^{-15}	0.1	3
Floor	0.01	3.6×10^{-14}	0.3	5
Aquifer	0.15	1.3×10^{-10}	0.5	2

begins to transfer and redistribute, which is specifically manifested in the concentration of compressive stress in the coal pillar in front of and behind the working face, and the tensile stress in a certain range is distributed in the roof and floor, and gradually increases with the increase of the mining distance. At the same time, the stress concentration at both ends of the hidden fault becomes more significant with the increase of the degree and scope of stress redistribution. When a hidden fault is present on the flat floor directly ahead of the working face, the pressure it experiences is transferred through the rock mass of the floor. This leads to a gradual build-up of stress within the fault, until reaching a maximum. During this time, as per the analysis, the fault is particularly prone to cracking and further expansion. Once the working face moves forward to extract the coal seam located above and in front of the fault, the floor rock mass is unloaded. At this point, the fault is no longer restricted from expanding longitudinally. Consequently, the highest extent of the fault's propagation is likely to be reached before the coal seam (above the fault) is mined away by the advancing working face.

When the working face recovers 20 m, 40 m, 60 m, and 80 m, the compressive stress and tensile stress

concentration of hidden fault occur at the end. However, when the working face is mined to 100 m, the hidden fault is located below the leading abutment pressure, and the compressive stress and tensile stress concentration position rise, and rises again when the working face is mined to 110 m. This phenomenon or the expansion of the hidden fault due to the crack initiation condition leads to the transfer of the stress concentration position at the fracture tip.

Figure 15 illustrated stress data of two survey lines in the mining process of the working face. It can be seen from the internal stress change of the hidden fault in Fig. 15a that due to the material heterogeneity of the fault fracture zone, the monitored stress data along the direction of the hidden fault are quite different, but from the stress change in the mining process, when the working face recovers 20 m, 40 m, 60 m, and 80 m, the stress of the hidden fault gradually increases, while when the working face recovers to 100 m or 110 m, the stress level of the hidden fault obviously decreases, This means that the hidden fault has been damaged or activated, and the internal bearing capacity of the hidden fault has been greatly reduced.

It can be seen from the stress data in Fig. 15 that when the distance is far from the working face, the stress in floor rock mass increases slowly and the tensile stress level at the fracture tip remains small. As mining operations reach ranges of 100 m to 110 m, the stress in the upper rock strata of the floor increases rapidly. This elevated stress gradually diminishes as it is transmitted to the deeper parts of the rock mass. However, at the end of the measurement line, there is a significant surge in tensile stress. This increase is closely related to the longitudinal development of hidden faults, as the peak tensile stress location at the tip of wing crack propagation indicates the

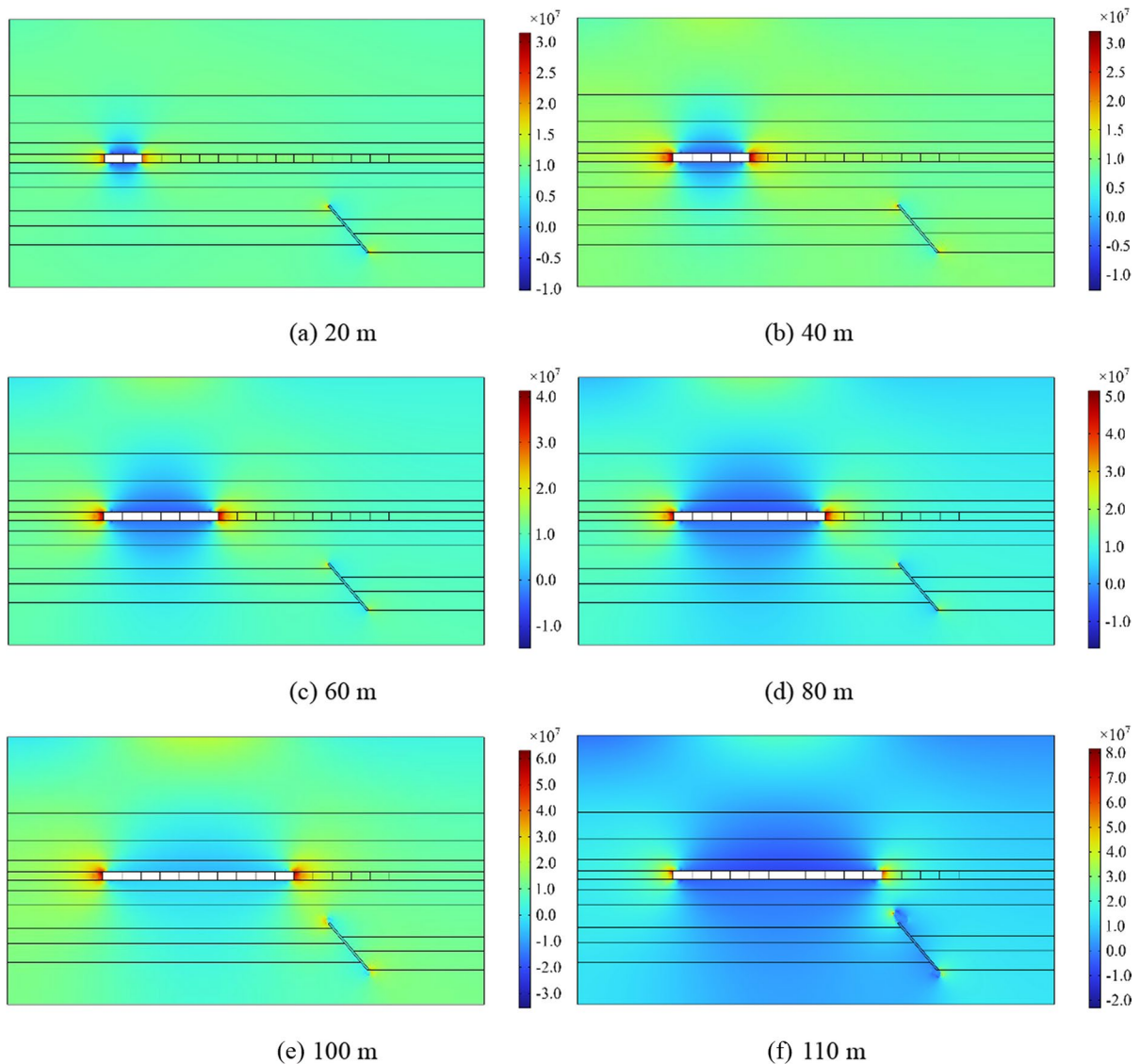


Fig. 14 Mean effective compressive stress (in [Pa]) distribution with varying mined distances

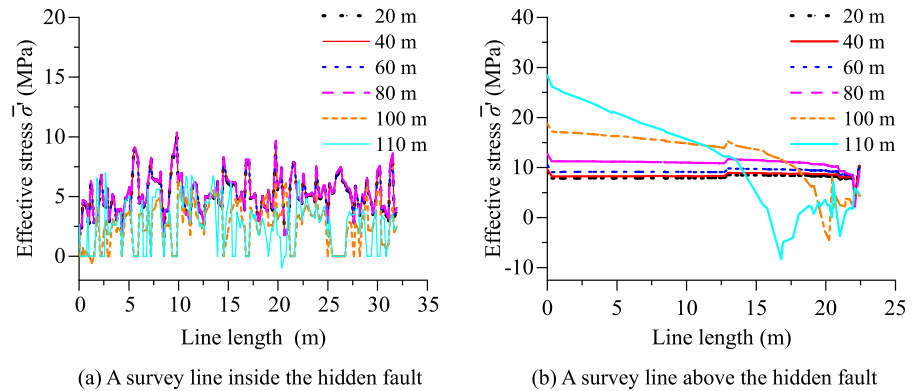
height at which the fractures have developed. Consequently, at a mining of 110 meters, the peak position of tensile stress is observed to be higher than in other conditions.

4.2 Evolution of damage zones

Figure 16 shows the distribution of damage variables during mining, reflecting the process and location of rock mass failure. It can be seen from the figure that the influence of the pushing mining of the working

face on the hidden fault of the floor is obvious. As a geological weak surface, when the hidden fault is recovered to 20 m, some damage has occurred inside the hidden fault. Of course, the actual situation is related to factors such as the nature of fillers inside the fault. In this model, the physical and mechanical properties of the simulated fault zone are weak, and damage is very easy to occur during mining. According to the stress, it can be known that it is a compression shear failure type. At the same time, the roof and floor of the working face are also subject to different

Fig. 15 Mean effective compressive stress along survey lines with varying mined distances



damage conditions. In the upper part of the goaf and the shallow part of the floor, the main damage is tensile damage, while in the vicinity of the coal wall, the main damage is the shear damage of oblique cutting, which together presents a “saddle” shaped damage area.

With the advance of the working face, the floor damage depth increases gradually, and the internal damage of the hidden fault also increases gradually. When the mining reaches 80 m, the hidden fault in the numerical simulation has almost been completely damaged, which can be understood as the activation of the original cementation state inside the fault. At this time, the floor damage depth reaches 13 m, and the hidden fault is still a certain distance from the floor damage zone. When the working face is mined to 100 m, the range of the floor failure zone expands, but the failure depth has remained stable, while the rock mass bearing capacity of the hidden fault gradually increases, the tensile stress concentration at the tip has met the tensile damage conditions, and the hidden fault starts to crack and expand. When the working face is recovered to 110 m, the hidden fault will further expand and connect with the floor failure zone, with a total extension length of 9.2 m. To this extent, a water inrush channel of “hidden fault to floor failure zone” has been formed to connect the floor confined aquifer with the working face.

4.3 Evolution of seepage field

The distribution of seepage pressure and seepage velocity before and after the formation of the water inrush channel is selected for the analysis of seepage field characteristics, as shown in Figs. 17 and

18. Before the formation of the water inrush channel, the seepage simulation is dominated by low velocity pore seepage, the confined water is guided upward along the top face of the aquifer, and the abnormal conductivity is formed by taking advantage of the natural permeability advantage of the hidden fault. If no hidden fault is detected on site, the water inrush coefficient calculated by the water inrush coefficient method is 0.093 MPa/m, which is less than the requirement of 0.1 MPa/m for normal blocks. However, the existence of hidden faults has great hidden danger for safe mining of the working face.

When the working face is advanced to 100 m, high water pressure has been rose near the hidden fault at the floor of the working face, but the simulation results still show low velocity seepage since no water inrush channel is formed. When the mining reaches 110 m, because a complete water inrush channel is formed at this moment, connecting the confined aquifer and the working face, the water pressure only decreases rapidly along the water inrush channel, which is converted into kinetic energy, forming a high-speed seepage channel, and the water inflow volume increases sharply, causing water inrush from the floor of the working face. However, in the actual situation, the floor crack is closed due to pressure. Meanwhile, the permeability is low, and there is no obvious water inrush. However, when the working face continues to advance, the floor crack rock mass is unloaded or further disturbed by mining, the crack opening increases, and the permeability increases sharply, often forming a lagging water inrush phenomenon.

To assess the status of the damage of the floor and to realize the early warning of the water inrush from floor, a microseismic monitoring device was installed

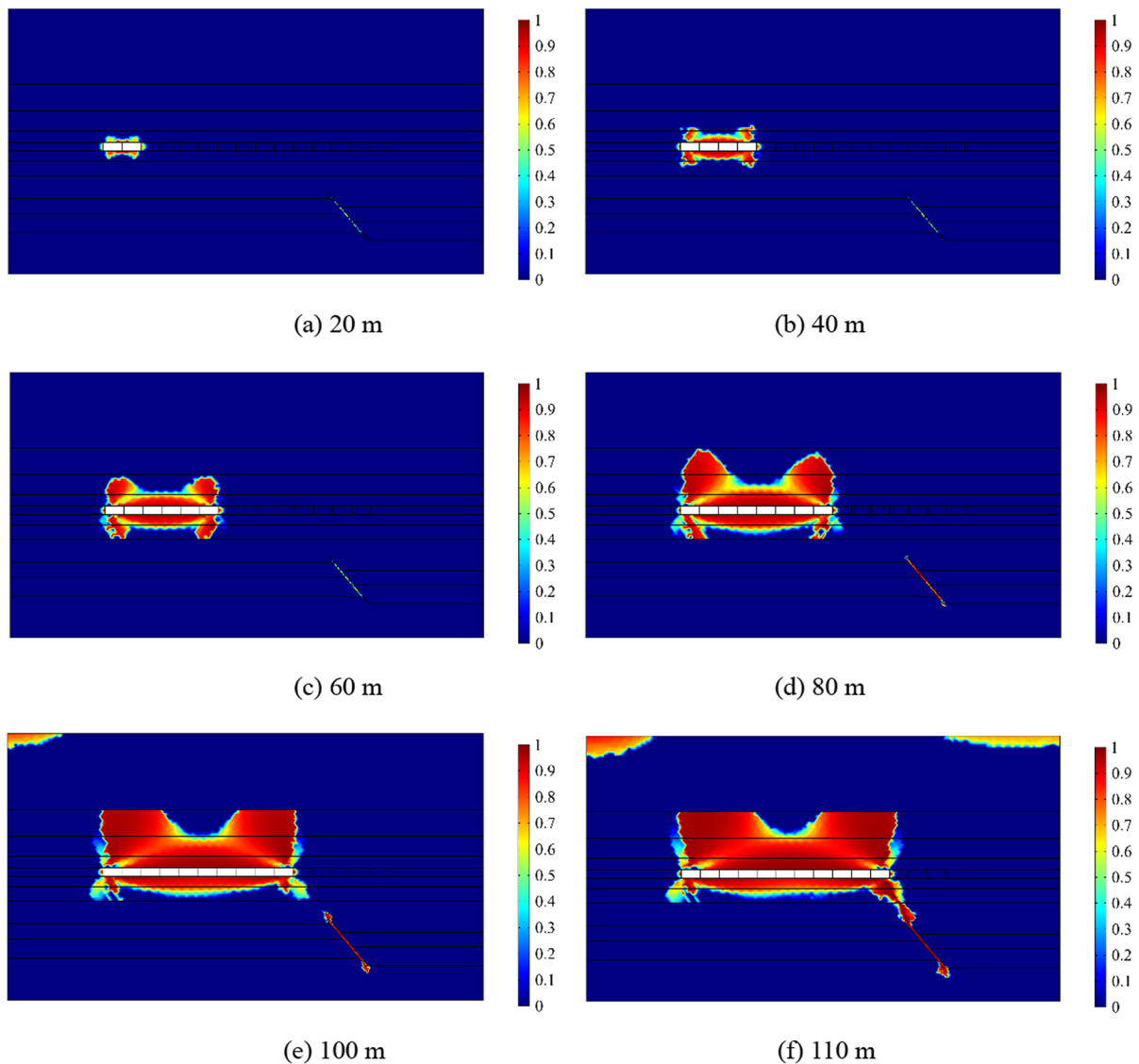


Fig. 16 Damage distribution with varying mined distances

in the roadway floor of the 27305 working face, and the geophone was connected to the data acquisition center by professional cables and optical fibers to realize the real-time monitoring. Figure 19 presents the microseismic monitoring results indicating microseismic events generated by the failure of the roof and floor caused by coal mining. Additionally, an inclined dense band of

microseismic events was observed in the deeper part of the floor, suggesting that the shallow floor damage zone has been connected with the deeper hidden faults and indirectly communicated with the aquifer below. The microseismic events monitoring results are consistent with the numerical analysis results, and preventive measures need to be taken at the site.

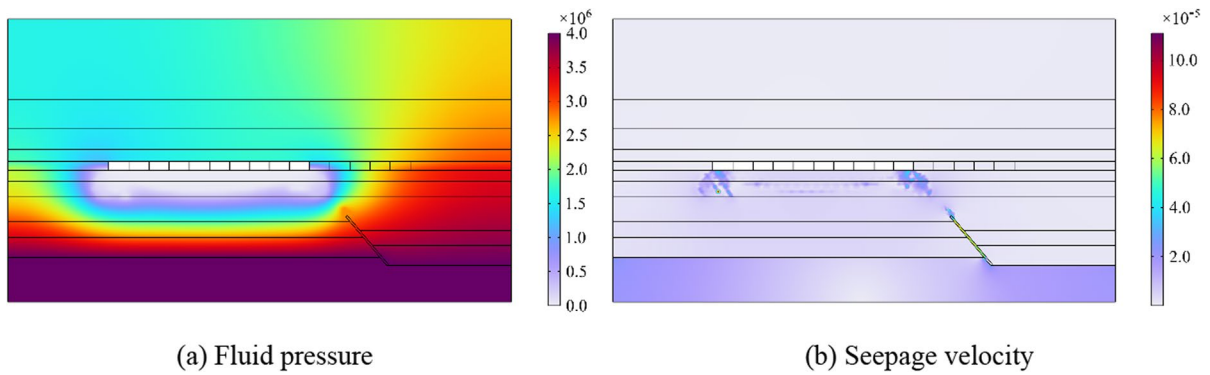


Fig. 17 Distribution of seepage field (the unit of fluid pressure is [Pa] and the unit of seepage velocity magnitude is [m/s]) at mined distance 100 m

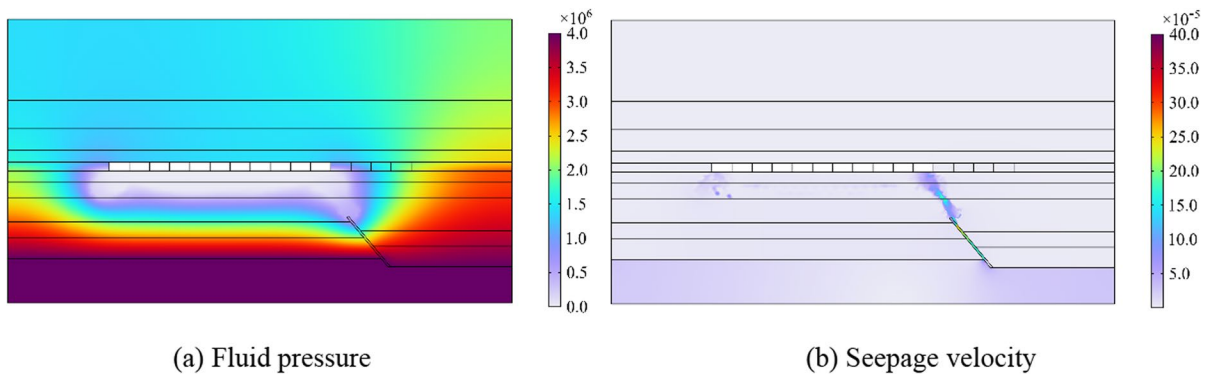
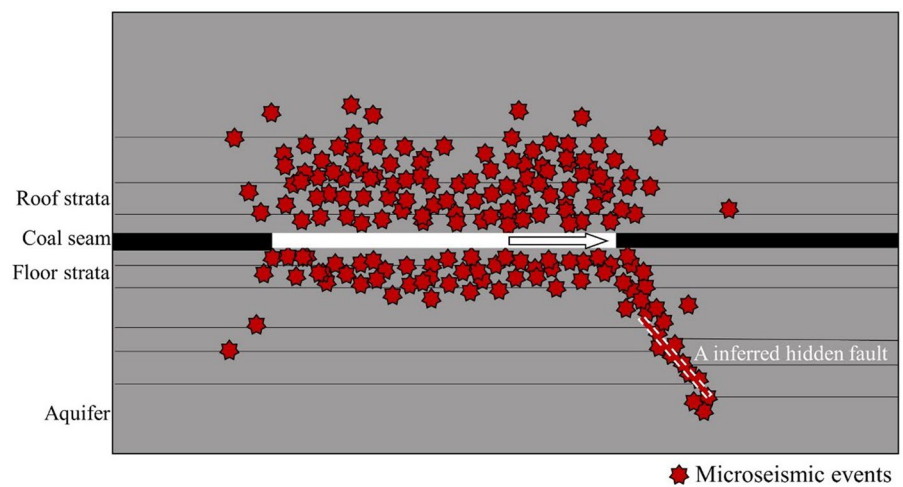


Fig. 18 Distribution of seepage field at mined distance 110 m (same units as before)

Fig. 19 Distribution of microseismic events near the working face



5 Discussions

5.1 The coupled stress–seepage–damage model for brittle rock materials

Hydro-mechanical coupling has been well recognized in geological activities, and rock damage and destruction caused by subsurface excavation under the coupling condition has also attracted attention (Lei et al. 2021; Zhao et al. 2021). Although rock failure modeling has been extensively studied (Zeng et al. 2019; Mondal et al. 2019; Zhou et al. 2020), the simulation of rock failure under coupled hydro-mechanical conditions is still a challenge. The proposed coupled stress–seepage–damage model is implemented by finite element method and can be used for discontinuity problems. In the biaxial compression test of rock samples under coupled stress–seepage conditions, the simulated samples experience the formation of final macroscopic shear fractured zones from random damage, and the permeability first decreases due to pore compaction and then increases with the evolution of damage, which are consistent with existing studies (Lu et al. 2013; Chen et al. 2017; Li and Liu 2021). In uniaxial compression test of a rock sample containing a pre-existing fracture under coupled stress–seepage conditions, the simulation results show a wing crack growth process consistent with the experiments (Wei et al. 2021), and the strengths of the samples all decrease with the increase of fluid pressure in the pre-existing fracture. The proposed model has been proved to be a simple and effective tool for simulating rock damage and fracture propagation under stress–seepage coupling conditions.

5.2 Water inrush from a hidden fault in coal mines

Hidden faults in the floor of coal seams, unlike large faults that cut diagonally through coal seams, have received less attention because of their small size and hidden nature. A few scholars have investigated the mechanism of water inrush from the hidden faults in the floor. Zhang et al. (2017) conducted physical simulations to study the process of water inrush from a hidden fault in the floor of the working face. The experiment revealed the mode of water inrush caused by the hidden fault connected to the destructive zone of the floor. However, the experiment did not provide detailed observations of the dynamic process of the

fracture propagation. Sun et al. (2019) simulated the process of water inrush from a hidden fault using the finite element method. However, the results only indicated that the base plate damage zone calculated by the Mohr–Coulomb criterion had covered the hidden fault. To evaluate the possibility of fault activation, Zhou et al. (2018) identified the stress concentration at the tip of a hidden fault and analyzed its stress intensity factor using the extended finite element method and fracture mechanics. This paper adds to the existing literature by demonstrating the process of fracture propagation of hidden faults in the floor during the mining process leading to water inrush.

5.3 Protection measures

This paper shows that hidden faults located in the floor of the working face can silently form water inrush channels during mining, which will pose a great threat to the mining operation if the hidden faults are not detected. For this kind of fracture propagation hidden in the floor, microseismic technology can effectively monitor the new failure situation and infer the distribution of fractured zones (Zhao et al. 2017; Yin et al. 2023), which plays a key role in understanding the formation of water inrush channels. Based on the water-richness data of the target area (Zhang and Wang, 2021), grouting is required when both high fluid pressure and fluid channels (fractured zones) are present. Through continuous grouting, the fractured zone of the floor is strengthened and the fracture network for fluid flow is gradually sealed until the water inflow is reduced from abnormal to normal.

6 Conclusions

In order to comprehensively analyze the evolution of water inrush induced by concealed fractures in the coal seam floor, this paper proposes a novel rock stress–seepage–damage coupling numerical model based on the poromechanics theory. This model effectively simulates the development of damage, propagation of fractures, and their interaction with fluid flow in rock materials. The model was implemented through the secondary development of the COMSOL Multiphysics simulation software, employing the finite element method. Furthermore,

the model's accuracy was validated through biaxial compression-seepage tests conducted on intact rock samples as well as rock samples with a pre-existing fracture.

To evaluate the practicality of the proposed model, it was applied to simulate the mining process at the 27305 working face in a mine located in Jining, Shandong Province. The simulation results successfully captured the process of spreading and evolution of water inrush from underlying faults during the mining operations. As the working face advances, an observed gradual increase in stress concentration at the end of the underlying fault is witnessed. The most critical scenario occurs when concealed faults are positioned beneath the working face, leading to a remarkable increase in the bearing compressive stress of these concealed faults until they reach the damage condition, subsequently causing fracture propagation. As the hidden fault extends into the damaged floor area, a water inrush passage forms, connecting the confined aquifer with the working space. Consequently, this initiates the evolution of floor water inrush disasters induced by the hidden fault.

Author contribution All authors contributed to the study conception and design. Material preparation, data collection and analysis were performed by Jianli Shao and Qi Zhang. The first draft of the manuscript was written by Jianli Shao. Wenquan Zhang reviewed the manuscript. All authors read and approved the final manuscript.

Funding This work was supported by the PhD Research Startup Foundation of Shandong Technology and Business University (Grant No. BS202310), the Hong Kong RGC Post-doctoral Fellowship Scheme (RGC Ref. No. PDFS2223-5S04), the PolyU Start-up Fund for RAPs under the Strategic Hiring Scheme (Grant No. P0043879), and the National Natural Science Foundation of China (Grant No. 52304235).

Data availability All data, models, or code generated or used during the study are available from the corresponding author upon reasonable request.

Declarations

Conflict of interest The authors have no competing interests to declare that are relevant to the content of this article.

Ethics approval Not applicable.

Consent to publish The authors confirm that their publication has been approved by all co-authors and the responsible authorities at the institution where the work is carried out.

Open Access This article is licensed under a Creative Commons Attribution 4.0 International License, which permits use, sharing, adaptation, distribution and reproduction in any medium or format, as long as you give appropriate credit to the original author(s) and the source, provide a link to the Creative Commons licence, and indicate if changes were made. The images or other third party material in this article are included in the article's Creative Commons licence, unless indicated otherwise in a credit line to the material. If material is not included in the article's Creative Commons licence and your intended use is not permitted by statutory regulation or exceeds the permitted use, you will need to obtain permission directly from the copyright holder. To view a copy of this licence, visit <http://creativecommons.org/licenses/by/4.0/>.

References

- Chen S, Yue ZQ, Tham LG (2004) Digital image-based numerical modeling method for prediction of inhomogeneous rock failure. *Int J Rock Mech Min Sci* 41:939–957. <https://doi.org/10.1016/j.ijrmms.2004.03.002>
- Cheng J, Sun X-Y, Zheng G et al (2013) Numerical simulations of water-inrush induced by fault activation during deep coal mining based on fluid-solid coupling interaction. *Disaster Adv* 6:10–14
- Chen X, Yu J, Tang C et al (2017) Experimental and numerical investigation of permeability evolution with damage of sandstone under triaxial compression. *Rock Mech Rock Eng* 50:1529–1549. <https://doi.org/10.1007/s00603-017-1169-3>
- Chen S, Wei C, Yang T et al (2018) Three-dimensional numerical investigation of coupled flow-stress-damage failure process in heterogeneous poroelastic rocks. *Energies* 11:1923. <https://doi.org/10.3390/en11081923>
- Du Y, Liu W, Meng X et al (2021) Effect of crack propagation on mining-induced delayer water inrush hazard of hidden fault. *Geofluids* 2021:1–12. <https://doi.org/10.1155/2021/6557578>
- Hu Y, Sun J, Liu W, Wei D (2019) The evolution and prevention of water inrush due to fault activation at working face no. II 632 in the Hengyuan Coal Mine. *Mine Water Environ* 38:93–103. <https://doi.org/10.1007/s10230-018-00579-w>
- Jirásek M, Bauer M (2012) Numerical aspects of the crack band approach. *Comput Struct* 110–111:60–78. <https://doi.org/10.1016/j.compstruc.2012.06.006>
- Kong H, Wang L (2020) The behavior of mass migration and loss in fractured rock during seepage. *Bull Eng Geol Environ* 79:739–754. <https://doi.org/10.1007/s10064-019-01581-4>
- Lei Q, Gholizadeh Doonechaly N, Tsang C-F (2021) Modeling fluid injection-induced fracture activation, damage growth, seismicity occurrence and connectivity change in naturally fractured rocks. *Int J Rock Mech Min Sci* 138:104598. <https://doi.org/10.1016/j.ijrmms.2020.104598>
- Lemaitre J (1985) A continuous damage mechanics model for ductile fracture. *J Eng Mater Technol* 107:83–89. <https://doi.org/10.1115/1.3225775>

- Li M, Liu X (2021) Experimental and numerical investigation of the failure mechanism and permeability evolution of sandstone based on hydro-mechanical coupling. *J Nat Gas Sci Eng* 95:104240. <https://doi.org/10.1016/j.jngse.2021.104240>
- Li L, Yang T, Liang L et al (2011) Numerical investigation of groundwater outbursts near faults in underground coal mines. *Int J Coal Geol* 85:276–288. <https://doi.org/10.1016/j.coal.2010.12.006>
- Li L, Xie D, Wei J et al (2020) Analysis and control of water inrush under high-pressure and complex karstic water-filling conditions. *Environ Earth Sci* 79:493. <https://doi.org/10.1007/s12665-020-09242-6>
- Li B, Wang X, Liu Z, Li T (2021) Study on multi-field catastrophe evolution laws of water inrush from concealed karst cave in roadway excavation: a case of Jiuyuan coal mine. *Geomat Nat Hazards Risk* 12:222–243. <https://doi.org/10.1080/19475705.2020.1870170>
- Liang Z, Song W (2021) Theoretical and numerical investigations of the failure characteristics of a faulted coal mine floor above a confined aquifer. *Mine Water Environ* 40:456–465. <https://doi.org/10.1007/s10230-021-00780-4>
- Liu J, Chen W, Nie W et al (2019) Experimental research on the mass transfer and flow properties of water inrush in completely weathered granite under different particle size distributions. *Rock Mech Rock Eng* 52:2141–2153. <https://doi.org/10.1007/s00603-018-1719-3>
- Liu C, Zhang P, Ou Y et al (2022) Analytical stress analysis method of interbedded coal and rock floor over confined water: a study on mining failure depth. *J Appl Geophys* 204:104720. <https://doi.org/10.1016/j.jappgeo.2022.104720>
- Lu Y, Wang L (2015) Numerical simulation of mining-induced fracture evolution and water flow in coal seam floor above a confined aquifer. *Comput Geotech* 67:157–171. <https://doi.org/10.1016/j.compgeo.2015.03.007>
- Lu YL, Elsworth D, Wang LG (2013) Microcrack-based coupled damage and flow modeling of fracturing evolution in permeable brittle rocks. *Comput Geotech* 49:226–244. <https://doi.org/10.1016/j.compgeo.2012.11.009>
- Ma D, Duan H, Zhang J (2022) Solid grain migration on hydraulic properties of fault rocks in underground mining tunnel: radial seepage experiments and verification of permeability prediction. *Tunn Undergr Space Technol* 126:104525. <https://doi.org/10.1016/j.tust.2022.104525>
- Mondal S, Olsen-Kettle L, Gross L (2019) Simulating damage evolution and fracture propagation in sandstone containing a preexisting 3-D surface flaw under uniaxial compression. *Int J Numer Anal Methods Geomech* 43:1448–1466. <https://doi.org/10.1002/nag.2908>
- Qian Z, Huang Z, Song J (2018) A case study of water inrush incident through fault zone in China and the corresponding treatment measures. *Arab J Geosci* 11:381. <https://doi.org/10.1007/s12517-018-3727-8>
- Rutqvist J, Wu Y-S, Tsang C-F, Bodvarsson G (2002) A modeling approach for analysis of coupled multiphase fluid flow, heat transfer, and deformation in fractured porous rock. *Int J Rock Mech Min Sci* 39:429–442. [https://doi.org/10.1016/S1365-1609\(02\)00022-9](https://doi.org/10.1016/S1365-1609(02)00022-9)
- Shao J, Zhang W, Wu X et al (2022) Rock damage model coupled stress-seepage and its application in water inrush from faults in coal mines. *ACS Omega* 7:13604–13614
- Sun W, Xue Y, Li T, Liu W (2019) Multi-field coupling of water inrush channel formation in a deep mine with a buried fault. *Mine Water Environ* 38:528–535. <https://doi.org/10.1007/s10230-019-00616-2>
- Tang CA, Tham LG, Lee PKK et al (2002) Coupled analysis of flow, stress and damage (FSD) in rock failure. *Int J Rock Mech Min Sci* 39:477–489. [https://doi.org/10.1016/S1365-1609\(02\)00023-0](https://doi.org/10.1016/S1365-1609(02)00023-0)
- Tang CA, Liang ZZ, Zhang YB et al (2008) Fracture spacing in layered materials: a new explanation based on two-dimensional failure process modeling. *Am J Sci* 308:49–72
- Wang B, Wu C, Kang L et al (2018) Work safety in China's Thirteenth Five-Year plan period (2016–2020): current status, new challenges and future tasks. *Saf Sci* 104:164–178. <https://doi.org/10.1016/j.ssci.2018.01.012>
- Wang Z, Zhang Q, Zhang W (2022) A novel collaborative study of abnormal roof water inrush in coal seam mining based on strata separation and wing crack initiation. *Eng Failure Anal* 142:106762. <https://doi.org/10.1016/j.engfailanal.2022.106762>
- Wang Z, Lian H, Liang W et al (2024) Experimental Study on the Fracture Process Zones and Fracture Characteristics of Coal and Rocks in Coal Beds. *Rock Mech Rock Eng* 57:1375–1393. <https://doi.org/10.1007/s00603-023-03620-9>
- Wei C, Zhang B, Zhu W et al (2021) Fracture propagation of rock like material with a fluid-infiltrated pre-existing flaw under uniaxial compression. *Rock Mech Rock Eng* 54:875–891. <https://doi.org/10.1007/s00603-020-02256-3>
- Weibull W (1951) A statistical distribution function of wide applicability. *J Appl Mech* 18:293–297. <https://doi.org/10.1115/1.4010337>
- Wu Q, Guo X, Shen J et al (2017) Risk assessment of water inrush from aquifers underlying the Gushuyuan Coal Mine, China. *Mine Water Environ* 36:96–103. <https://doi.org/10.1007/s10230-016-0410-8>
- Xu T, Yang S, Chen C et al (2017) Numerical investigation of damage evolution and localized fracturing of brittle rock in compression. *J Perform Constr Facil* 31:04017065. [https://doi.org/10.1061/\(ASCE\)CF.1943-5509.0001061](https://doi.org/10.1061/(ASCE)CF.1943-5509.0001061)
- Yang TH, Tham LG, Tang CA et al (2004) Influence of heterogeneity of mechanical properties on hydraulic fracturing in permeable rocks. *Rock Mech Rock Eng* 37:251–275. <https://doi.org/10.1007/s00603-003-0022-z>
- Yin H, Zhang G, Wu Q et al (2023) A deep learning-based data-driven approach for predicting mining water inrush from coal seam floor using microseismic monitoring data. *IEEE Trans Geosci Remote Sens* 61:1–15. <https://doi.org/10.1109/TGRS.2023.3300012>
- Zeng Q-D, Yao J, Shao J (2019) Study of hydraulic fracturing in an anisotropic poroelastic medium via a hybrid EDFM-XFEM approach. *Comput Geotech* 105:51–68. <https://doi.org/10.1016/j.compgeo.2018.09.010>
- Zhang Q, Wang Z (2021) Spatial prediction of loose aquifer water abundance mapping based on a hybrid statistical learning approach. *Earth Sci Inform* 14:1349–1365. <https://doi.org/10.1007/s12145-021-00640-3>

- Zhang R, Jiang Z, Zhou H et al (2014) Groundwater outbursts from faults above a confined aquifer in the coal mining. *Nat Hazards* 71:1861–1872. <https://doi.org/10.1007/s11069-013-0981-7>
- Zhang S, Guo W, Li Y et al (2017) Experimental simulation of fault water inrush channel evolution in a coal mine floor. *Mine Water Environ* 36:443–451. <https://doi.org/10.1007/s10230-017-0433-9>
- Zhang S, Shen B, Li Y, Zhou S (2019) Modeling rock fracture propagation and water inrush mechanisms in underground coal mine. *Geofluids* 2019:1–15. <https://doi.org/10.1155/2019/1796965>
- Zhang Q, Borja RI. Poroelastic coefficients for anisotropic single and double porosity media. *Acta Geotech.* 2021;16:3013–3025. <https://doi.org/10.1007/s11440-021-01184-y>
- Zhao Y, Yang T, Zhang P et al (2017) The analysis of rock damage process based on the microseismic monitoring and numerical simulations. *Tunn Undergr Space Technol* 69:1–17. <https://doi.org/10.1016/j.tust.2017.06.002>
- Zhao J, Bo L, Juntao C, Ning J (2020a) Mechanism of seepage-stress fault water inrush and grouting seal. *Arab J Geosci* 13:404. <https://doi.org/10.1007/s12517-020-05319-5>
- Zhao J, Zhang X, Jiang N et al (2020b) Porosity zoning characteristics of fault floor under fluid–solid coupling. *Bull Eng Geol Environ* 79:2529–2541. <https://doi.org/10.1007/s10064-019-01701-0>
- Zhao C, Zhang Z, Lei Q (2021) Role of hydro-mechanical coupling in excavation-induced damage propagation, fracture deformation and microseismicity evolution in naturally fractured rocks. *Eng Geol* 289:106169. <https://doi.org/10.1016/j.enggeo.2021.106169>
- Zhao J, Liu W, Shen J et al (2022) A real-time monitoring temperature-dependent risk index for predicting mine water inrush from collapse columns through a coupled thermal–hydraulic–mechanical model. *J Hydrol* 607:127565. <https://doi.org/10.1016/j.jhydrol.2022.127565>
- Zhou Q, Herrera J, Hidalgo A (2018) The numerical analysis of fault-induced mine water inrush using the extended finite element method and fracture mechanics. *Mine Water Environ* 37:185–195
- Zhou S, Zhuang X, Rabczuk T (2020) Phase field method for quasi-static hydro-fracture in porous media under stress boundary condition considering the effect of initial stress field. *Theor Appl Fract Mech* 107:102523. <https://doi.org/10.1016/j.tafmec.2020.102523>
- Zhu WC, Wei CH (2011) Numerical simulation on mining-induced water inrushes related to geologic structures using a damage-based hydromechanical model. *Environ Earth Sci* 62:43–54. <https://doi.org/10.1007/s12665-010-0494-6>
- Zuo J, Wu G, Du J et al (2022) Rock strata failure behavior of deep ordovician limestone aquifer and multi-level control technology of water inrush based on microseismic monitoring and numerical methods. *Rock Mech Rock Eng* 55:4591–4614. <https://doi.org/10.1007/s00603-022-02891-y>

Publisher's Note Springer Nature remains neutral with regard to jurisdictional claims in published maps and institutional affiliations.